A reconfigurable and automatic platform for the on-demand production of stretchable conductive composites

OPEN ACCESS
IOP Publishing
Smart Materials and Structures
Smart Mater. Struct. **32** (2023) 045018 (10pp)
https://doi.org/10.1088/1361-665X/acc221

A reconfigurable and automatic platform for the on-demand production of stretchable conductive composites

Hongda Lu[1], Qingtian Zhang[1], Xumin Huang[3], Tim Cole[2], Guolin Yun[4], Yuxin Zhang[2], Ruirui Qiao[3], Weihua Li[1,*] and Shi-Yang Tang[2,*]

[1] School of Mechanical, Materials, Mechatronic and Biomedical Engineering, University of Wollongong, Wollongong, NSW 2522, Australia
[2] Department of Electronic, Electrical and Systems Engineering, University of Birmingham, Edgbaston, Birmingham B15 2TT, United Kingdom
[3] Australian Institute for Bioengineering and Nanotechnology, University of Queensland, St Lucia, QLD 4072, Australia
[4] Department of Engineering, University of Cambridge, The Old Schools, Trinity Ln, Cambridge CB2 1TN, United Kingdom

E-mail: weihuali@uow.edu.au and S.Tang@bham.ac.uk

Received 28 October 2022, revised 15 February 2023
Accepted for publication 7 March 2023
Published 20 March 2023

Abstract

Stretchable conductive composites (SCCs) have been widely used as interconnects and sensors in stretchable electronic devices due to their tunable electromechanical properties and intrinsically high stretchability compared to solid metals. SCCs can be readily made by mixing (or breaking bulk) conductive fillers within an elastomeric polymer, which are subsequently cured. Despite the simplicity of this, most fabrication methods follow customized protocols and lack precise automatic control. These methods also require bulky and costly equipment (e.g. stirrers, mixers, ovens, and vacuuming machines). Also, variations in the production process make it challenging to maintain the consistency of SCC's electrical and mechanical properties produced in different batches. To solve this problem, this work develops an automatic SCC production platform (ASPP) that can be programmed to produce SCCs with high consistency in properties. The versatility of ASPP is demonstrated by fabricating SCCs with single and hybrid fillers, and porous structures. The consistency of SCCs' electromechanical properties is examined using samples fabricated in different batches following the same protocol. We further utilize the fabricated SCCs to realize various intelligent tactile sensing and heating platforms. The capability demonstrated for the ASPP shows its potential in fabricating SCCs for applications in soft robotics and wearable devices.

Supplementary material for this article is available online

Keywords: automatic platform, liquid metal, stretchable composites, soft electronics

(Some figures may appear in colour only in the online journal)

* Authors to whom any correspondence should be addressed.

1. Introduction

Stretchable composites, especially stretchable conductive composites (SCCs) using elastomeric matrices with conductive fillers, have promoted applications in soft robotics [1, 2], electronics [3–7], and sensors [8] based on their thermal, electrical, and mechanical properties. In general, elastomeric matrices are nonconductive and mainly contribute to mechanical properties such as tensile strength, Young's modulus, and stretch limit. Their mechanical properties usually stem from the polymer networks inside by chemically or physically crosslinking. For instance, silicones have stable mechanical structures due to their polymer chains connected by chemical covalent bonds. Poly (dimethlysiloxane) (PDMS) and Ecoflex are common silicones used in stretchable electronics [9–13] and sensing [14–16]. Fillers dispersed into the matrices are mainly responsible for electrical properties and have a synergetic effect together with matrices on mechanical properties [17, 18].

Metallic and nonmetallic conductive fillers such as silver [19–21], nickel [22–24], iron [25], carbon nanotubes [26, 27], and graphene [28–30] are commonly incorporated into elastomeric matrices to make SCCs. However, the soft-rigid interfaces in such composites during stretching, twisting or bending may form irreversible cracks and delamination to degrade electrical and mechanical properties [31]. SCCs with single fillers need to make trade-offs between mechanical and electrical properties due to the limited deformation of rigid particles. Increased filler content will result in greater electrical conductivity for the composite at the cost of increased stiffness. Ga-based liquid metals (LMs) such as eutectic gallium indium (EGaIn) are introduced to overcome the drawbacks. Bestowed with excellent properties such as low toxicity, low viscosity, good thermal conductivity, shape reconfigurability, and conductivity [32], LM-based SCCs (LM-SCCs) not only provide conductive paths but also retain the elastic property of the matrices. LM-SCCs have shown promising applications in flexible transient electronics [33, 34], actuators [35], self-healing devices [36], and transistors [37]. Moreover, LM-SCC with porous structures have been developed to show their potential in lightweight intelligent devices [38], energy harvesting [39], sensing [40, 41], and making conductors [42].

Apart from the matrix and the filler, the fabricating process also impacts the electrical and mechanical properties, such as Young's modulus, tensile strength, and electrical conductivity. To date, various methods have been developed to fabricate LM-SCCs, which involve processes that break bulk LM into micro/nano-sized droplets, such as direct mixing [43], solution mixing [44], and sonication [45, 46]. The elastomer-LM mixture is subsequently patterned using spin coating [47], direct printing [48], and mold casting [14] techniques at a designed temperature. And yet, the above-mentioned fabrication methods follow customized protocols and lack precise automatic control. These methods also require various equipment like magnetic stirrers, mixers, ovens, and vacuuming machines, which are space occupied. As for material transfer between different equipment, such a process is labor intensive and unavoidably causes material loss, which compromises productivity. Moreover, from batch to batch, variations in the production process make maintaining the consistency of SCC's electrical and mechanical properties challenging. Therefore, a universal platform that can automatically achieve the on-demand and repeatable fabrication of SCCs is crucial for developing devices with desired properties and consistent performance, thereby enabling researchers with different expertise backgrounds to utilize the advantages of SCCs in expanding their fields of research and interdisciplinary innovations.

To overcome this challenge, here, we design and construct an automatic SCC production platform (ASPP) using functional modules (mixing, vacuuming, and curing) for the fabrication of SCCs with desired properties and batch-to-batch consistency. We demonstrate the fabrication of SCCs with single and hybrid fillers, and examine their consistency in electromechanical properties using samples fabricated in different batches following the same protocol. We further examine the capability of the ASPP for fabricating porous composites. The excellent electromechanical performance of the fabricated SCC is demonstrated by applying them to realize intelligent platforms such as Morse code tapping, tactile sensing, and self-regulated heating devices. We believe that the ASPP will facilitate the adoption and enable the vast potential of SCCs in soft electronics, wearable devices, and biomedical applications.

2. Results and discussion

2.1. Development of the ASPP

Figure 1(a) shows the structure of the ASPP. The platform mainly consists of a *XYZ* motorized stage, a proportional-integral-derivative (PID) temperature control (TC) module, a cooling sink, a thermocouple sensor plugged in a slidable holder, a Peltier cooler pad, a vacuum pump (∼80 kPa) connected to a container, and a DC motor (maximum 9000 rpm) assembled with a replaceable agitator (see figure S1 for details). The *XYZ* motorized stage consists of a controller containing three A4988 stepper motor driver carriers, three stepping motors, and guide rails. The PID TC module includes a H-bridge to regulate the current directions for the Peltier cooler pad; an eight-digit light emitting diode display to show real-time temperature, target temperature, and working time; and a microcontroller board (Arduino Mega 2560) to read the feedback signals from the thermocouple and output the driving signals in real-time based on the PID control algorithm. Details of the TC module can be found in figure S2 [49]. The container is placed on the slidable holder, with one side attached to the Peltier cooler pad using silicone thermal paste (the exploded view is shown in the left inset of figure 1(a)). The other side of the Peltier cooler pad connects to a cooling sink. Switching the polarity of the current passing through the Peltier cooler pad can heat or cool the container effectively. Figure 1(b) shows

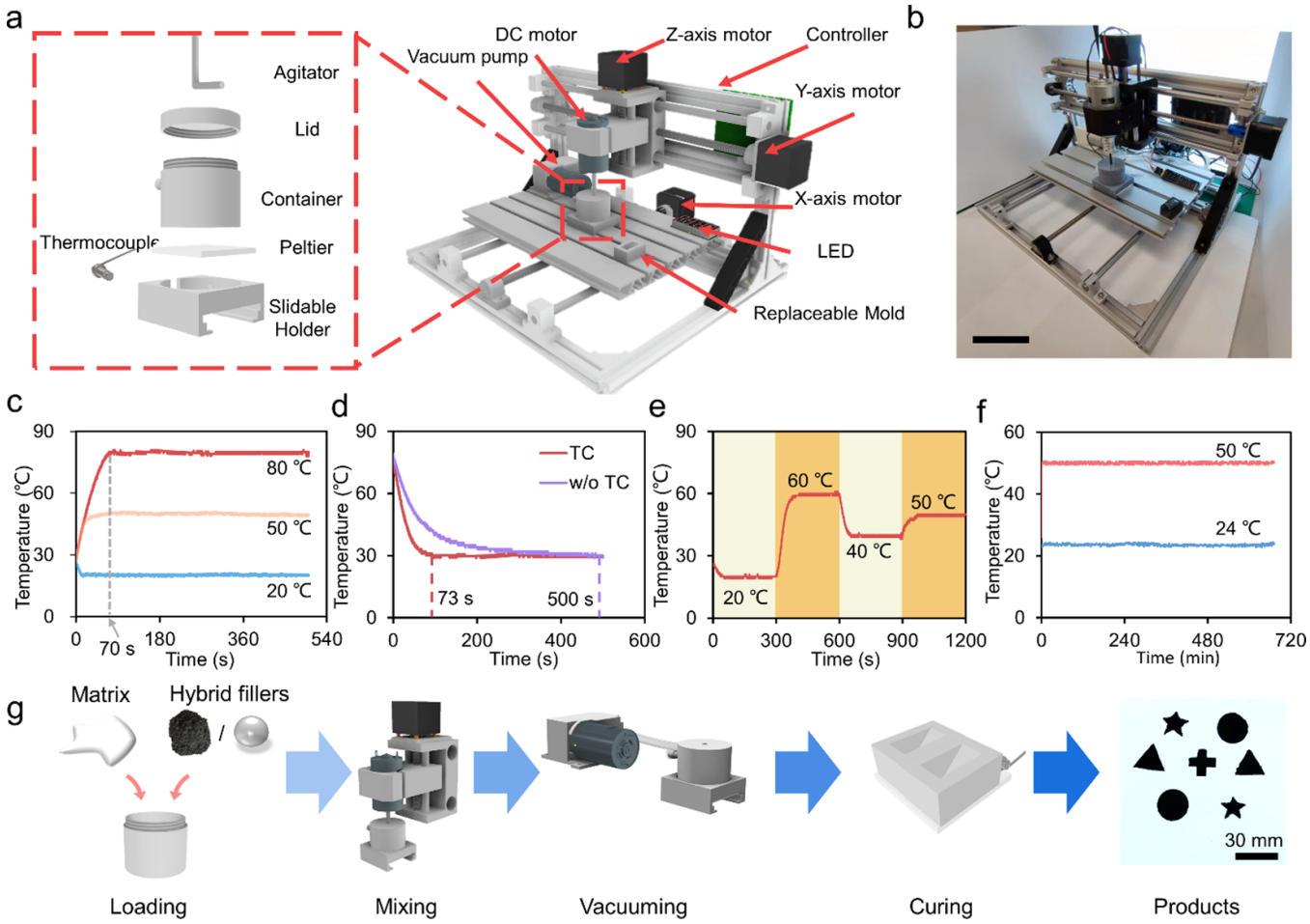

Figure 1. Design and performance of the ASPP. (a) Schematics of the ASPP. The left inset is the exploded schematic representation for the container in the holder with the TC module. (b) Actual image of the assembled ASPP. Scale bar is 10 cm. (c) Temperature *vs* time plots for water in the container with different target temperatures. (d) Cooling of water inside the container with and without using the TC module. (e) Dynamic temperature control using the TC module. (f) Long-term temperature stability test using the TC module. (g) Schematic diagrams showing the fabricating process of SCCs using the ASPP.

the actual ASPP. All modules are commercially available, and the total cost of the platform is less than $500 (see table S1 for details).

Controlling the temperature is essential to prevent early-stage curing of the elastomeric matrix caused by increased temperature during the mixing process [11]. Maintaining the temperature is also important in the curing stage of the fabrication process to yield SCCs with desired properties. Therefore, we optimize the PID coefficients to adjust the temperature on demand and avoid fluctuation and overshoot. We add water to the container and activate the agitator to simulate the operating condition. By setting different target temperatures of 20 °C, 50 °C, and 80 °C, we demonstrate that the ASPP can achieve precisely and instantly TC, as evidenced by the monitored temperature versus time plots depicted in figure 1(c). The TC module allows the liquid in the container to reach target temperatures in less than 70 s and maintain them stably. In addition to heating, we test the module to cool liquid in the container down from 80 °C to 30 °C and compare it with the case without TC (w/o TC). The cooling rate can be ∼6 times faster with the TC module, as shown in figure 1(d). Apart from the steady TC, the ability of dynamic TC is further investigated. We program the TC module to continuously heat up and cool down water in the container to different temperatures and keep it steady for 300 s, as depicted in figure 1(e). Furthermore, the TC module allows the container to maintain at 24 °C and 50 °C for over 10 h despite the ambient temperature fluctuation (figure 1(f)), verifying the stability of the TC module for long-term operation to meet the requirement for the fabrication of various SCCs.

Apart from TC, the *XYZ* motorized stage automatically moves the agitator to programmed positions, enabling thorough and controlled mixing. With the same settings, the fabricated SCCs can maximally retain the desired electrical and mechanical properties. The vacuum pump is responsible for removing air bubbles trapped in the uncured mixture during the mixing process. The ASPP automatically follows the steps of loading, mixing, vacuuming, and curing for fabricating SCCs, as shown in figure 1(g). With customized molds, SCCs with different shapes can be obtained (see figure 1(g)).

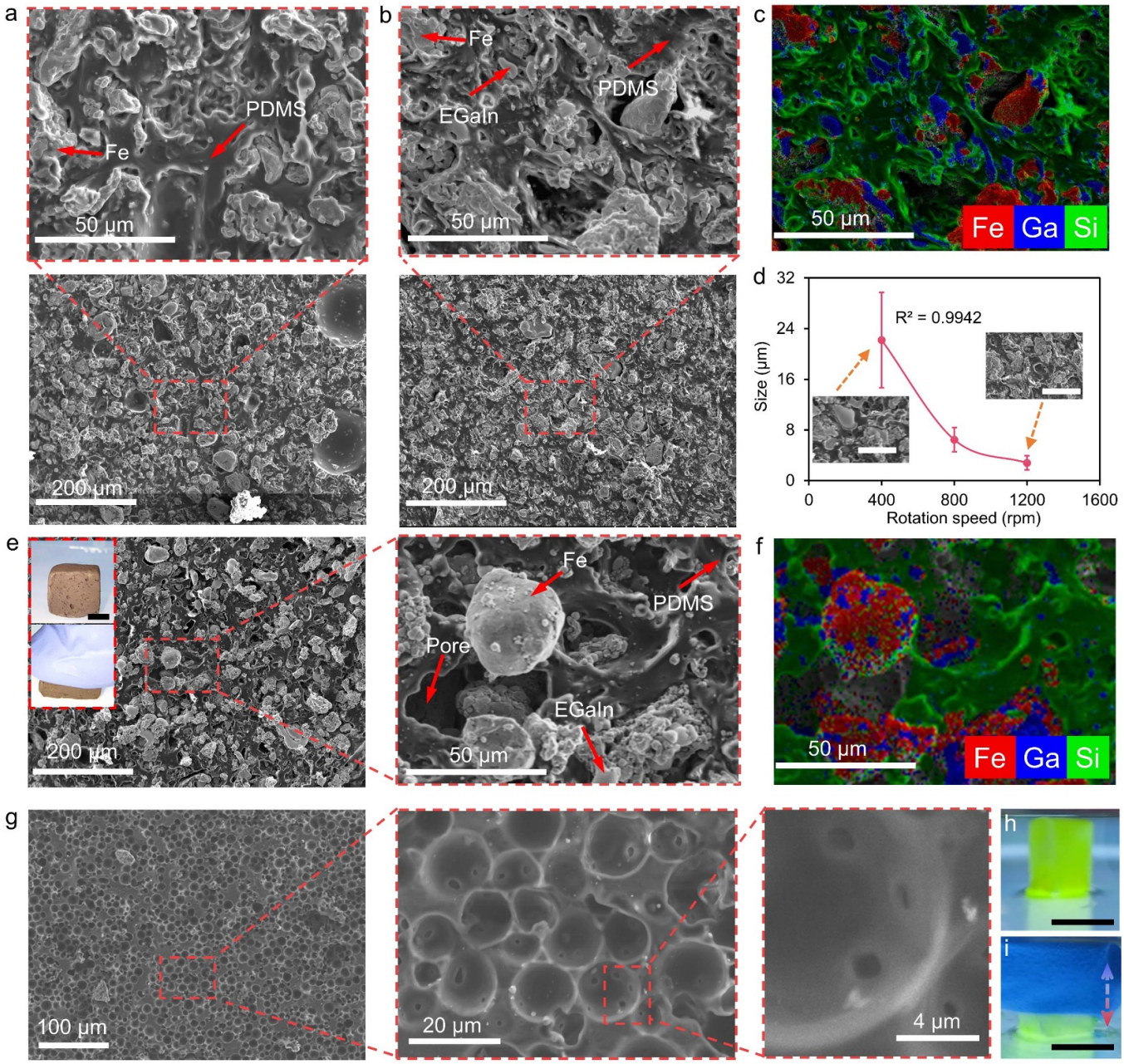

Figure 2. Production of SCCs using the ASPP. (a) SEM images of the obtained P_{Fe4}. (b) Average sizes of EGaIn droplets in $P_{Fe4\text{-}LM}$ *vs* rotating speed of the agitator. The insets are SEM images of the $P_{Fe4\text{-}LM}$ corresponding to different rotation speeds. Scale bars are 50 μm. (c), (d) SEM images and EDS mapping of the obtained $P_{Fe4\text{-}LM}$. (e), (f) SEM images and EDS mapping of the obtained porous $P_{Fe4\text{-}LM}$. The inset shows the porous SCC can be readily compressed. Scale bar is 5 mm. (g) SEM images of the large and small pores of the porous PDMS. (h)–(i) A sponge made from the porous PDMS filled with water that contains a fluorescein sodium salt. Scale bar is 5 mm.

2.2. Production of SCCs using the ASPP

Taking advantage of the ASPP, we first make SCCs with single fillers. Briefly, we add the PDMS base, curing agent, and Fe powders (325 mesh) with a weight ratio of 1:0.1:4 in the container and subsequently activate the ASPP to fabricate the PDMS-Fe SCC (P_{Fe4}). The Fe powders distribute uniformly within the PDMS matrix, as shown in the scanning electron microscopy (SEM) images given in figure 2(a). The fabrication of SCCs using a different silicone elastomer of Ecoflex is also tested. The electrical and mechanical properties of these SCCs will be discussed in detail in the next section.

We also test the fabrication of hybrid-filler SCCs using the ASPP. Similarly, we simply add PDMS base, curing agent, Fe powders, and EGaIn with a weight ratio of 1:0.1:4:1 in the container and activate the ASPP to automatically fabricate the PDMS-Fe-EGaIn SCC ($P_{Fe4\text{-}LM}$). All materials are uniformly distributed, as shown in the SEM images given in figure 2(c). Figure 2(d) (see also figure S3) shows the energy dispersive x-ray spectroscopy (EDS) mapping of Fe, Ga, and Si for

the red dashed area in figure 2(c). Bulk EGaIn is broken into microdroplets (<30 μm) during the mixing process. Since the EGaIn droplet size affects the electrical and mechanical properties of the composite [25, 50], it is necessary to investigate if the ASPP is capable of fabricating SCCs with controlled EGaIn droplet sizes. We program the ASPP to operate at different rotating speeds (400, 800, and 1200 rpm) to provide different shear forces for breaking bulk EGaIn while keeping other parameters the same. Figure 2(b) shows that the size of the EGaIn droplets in the produced composites is inversely proportional to the rotating speed ($R^2 = 0.9942$). Also, a higher mixing speed leads to a more uniform size distribution.

We further demonstrate the versatility of the ASPP by fabricating porous SCCs with hybrid fillers. Previous research has shown that porous SCCs can be used to make capacitive pressure sensors with high sensitivity and power efficiency [51]. To fabricate porous SCCs, we remove the vacuuming module and activate the ASPP to stir a mixture containing PDMS base, curing agent, Fe powders, and EGaIn (weight ratio of 1:0.1:4:1) in the container for 3 min. Next, a quarter volume of glycerol and Polysorbate 20 non-ionic surfactant (weight ratio 19:1) is added into the container to further mix for 5 min at room temperature. The mixture is then heated to 50 °C to cure. The porous $P_{Fe4\text{-}LM}$ is finally obtained by removing glycerol by dissolving it in water. Uniform distribution of all materials can be observed, as shown in the SEM images given in figure 2(e). Figure 2(f) (see also figure S4) shows the EDS mapping of Fe, Ga, and Si for the red dashed area in figure 2(e).

In addition to SCCs, the ASPP is also capable of fabricating porous PDMS sponges. PDMS sponges have shown their applications in drug release for chemical stimulation of cells [52, 53]. Similar to the fabrication process of porous SCCs, glycerol and Polysorbate 20 non-ionic surfactant (weight ratio of 19:1) are firstly added into the container and thoroughly mixed for 3 min. Next, the same volume of mixture that contains PDMS base, curing agent, and monohydroxy terminated PDMS (weight ratio of 15:2:5) is added into the container. The mixture is further mixed for 10 min and the TC module keeps it at room temperature. The composite is then heated up to 50 °C to cure. The final PDMS porous sponge is obtained by putting the cured mixture into deionized water to remove glycerol. SEM images given in figure 2(d) show the highly porous structure, in which we can see that small pores (<2 μm) can form within large pores (23.21 ± 8.52 μm), leading to a high porosity of 62%. The porous PDMS can act as a sponge to absorb fluorescent dye solution, as shown in figures 2(f) and (g).

2.3. Electrical and mechanical properties of the produced SCCs

We characterize the mechanical and electrical properties of samples made in different batches to demonstrate the ability of the ASPP to fabricate SCCs with high consistency. SCC samples with different weight ratios of elastomer (PDMS or Ecoflex) to Fe powders from 1:1 to 1:4 are fabricated (denoted as $P_{Fe1/2/3/4}$ and $E_{Fe1/2/3/4}$, respectively). The measured Young's modulus for three $P_{Fe1/2/3/4}$ and PDMS samples are shown in figure 3(a), from which we can see that samples with the same PDMS to Fe ratio exhibit a similar Young's modulus (coefficient of variation (CV) < 6.21%), indicating the consistency of SCCs made by the ASPP. Similar results are obtained for $E_{Fe1/2/3/4}$, as shown in figure S5. Increasing the content of Fe fillers leads to a higher Young's modulus. We subsequently analyze the consistency of electrical properties for the samples by measuring the change of resistance in response to compression strain. Figures 3(b) and (c) show the resistivity-compression strain curves obtained for P_{Fe4} and E_{Fe4} samples, respectively, fabricated in three batches. A very similar response to compressive strain is observed, which further verifies the ability of the ASPP to fabricate SCCs with batch-to-batch consistency. Similar to the compression testing results, we observe that the resistivity of the SCCs also decreases exponentially with the growth of the tensile strain (see figure S6), indicating that the SCCs exhibit positive piezoconductivity similar to our previously reported conductive composites [25, 54]. The porous $P_{Fe4\text{-}LM}$ shows lower sensitivity to compression strain compared with non-porous SCCs, as shown in figure S7.

As the compression strain increases, the resistivity of both P_{Fe4} and E_{Fe4} drop exponentially due to the increased number of conductive pathways generated by the connected Fe particles. At the compression strain of 0.2, the resistivity of P_{Fe4} drops over 1000 times, which is more drastic than that of E_{Fe4}. Figure 2(d) shows the resistivity changes of P_{Fe4} during a cyclic compressing experiment. We pre-compress P_{Fe4} to 2 MΩ and then apply cyclic compression strain from 0 to 0.1. It is noticeable that the resistance decreases sharply during compression and can restore to the initial value, indicating good cyclic stability of P_{Fe4}. E_{Fe4} also exhibits excellent durability (see figure S8). For SCCs with hybrid fillers of Fe and EGaIn microdroplets, our results show that samples prepared in different batches also exhibit consistent performance, as shown in figure 3(e). An exponential decrease of resistivity is observed for $P_{Fe4\text{-}LM}$, where decreasing the EGaIn droplet size (using a higher stirring speed) leads to a higher resistivity under the same strain. We further measure the tensile limits of $P_{Fe1/2/3/4}$ and $E_{Fe1/2/3/4}$, as shown in figures 3(f) and S9, respectively. Generally, the rupture strain decreases with the increase in Fe particle content for both SCCs with different elastomer matrices. Also, SCCs with Ecoflex have higher tensile limits due to the greater stretchability and lower Young's modulus of Ecoflex.

Next, we characterize the strain–stress behaviors of the SCCs using cyclic loadings by gradually increasing the maximum compression strain. Figures 3(g)–(i) and (j)–(l) show the results obtained for composites using PDMS and Ecoflex, respectively. All samples show the Mullins effect [55] and the increase in the content of Fe powder filler renders more obvious elastic hysteresis. Meanwhile, we can see that Young's modulus of each sample in the unloading period decreases with the increase in the maximum loading. In addition, stress–strain curves for cyclic loadings with the same maximum compression strain are obtained (see figure S10). The curves become stable and start overlapping from the second cycle.

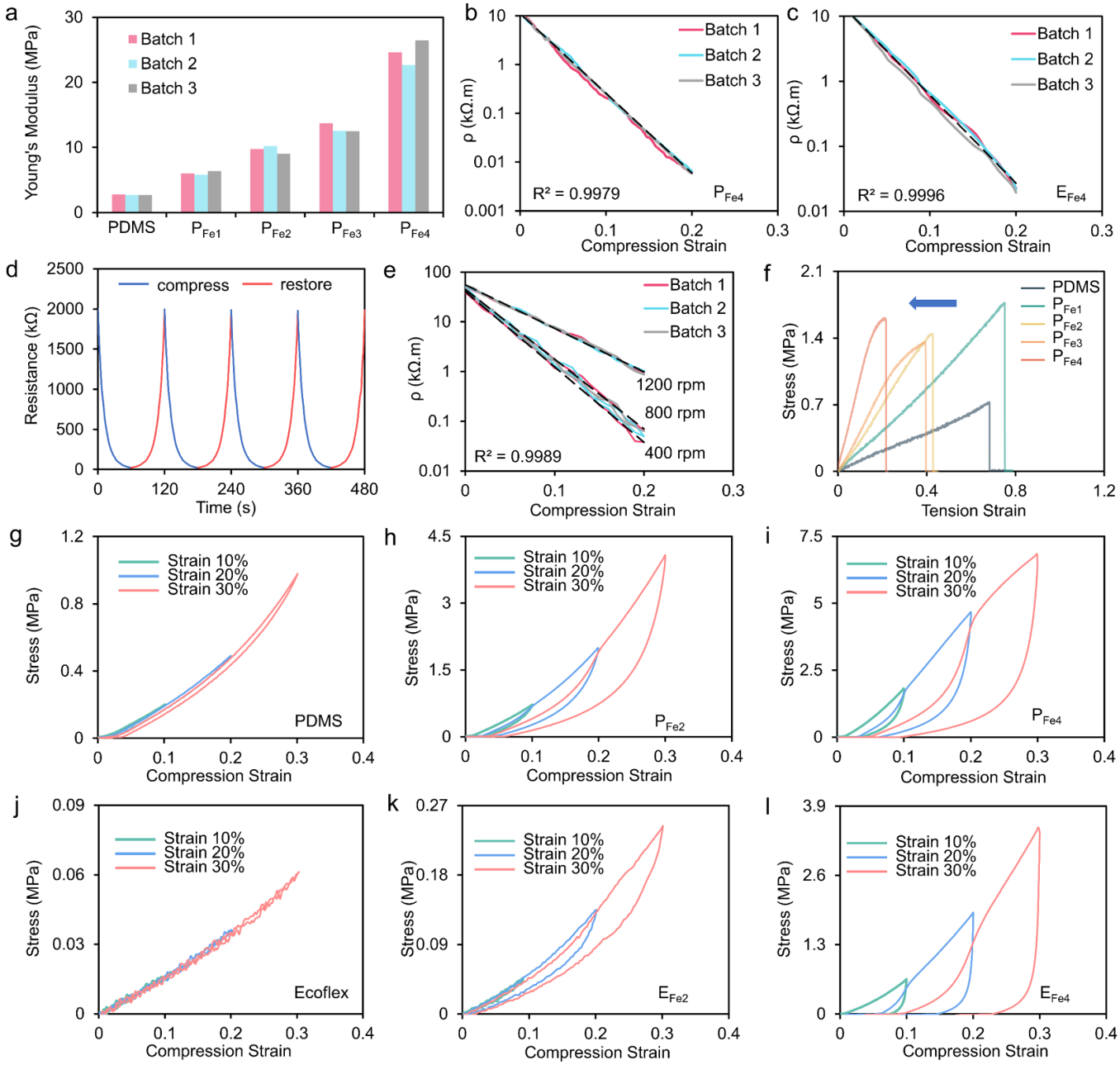

Figure 3. Electrical and mechanical properties of SCCs. (a) Young's modulus of PDMS and $P_{Fe1/2/3/4}$ samples fabricated from three different batches using the ASPP. Electrical resistivity *vs*. strain curves obtained for (b) P_{Fe4} and (c) E_{Fe4} samples. (d) Resistance *vs* time plots for four cyclic loadings of P_{Fe4}. (e) Changes of electrical resistivity in response to the compressive strain for the $P_{Fe4\text{-}LM}$ obtained using different rotation speeds from three different batches. (f) Stress–strain curves for measuring the tensile limit of PDMS and $P_{Fe1/2/3/4}$. Cyclic compressive loading and unloading plots with increased strains for (g) PDMS, (h) P_{Fe2}, (i) P_{Fe4}, (j) Ecoflex, (k) E_{Fe2}, and (l) E_{Fe4}.

In addition to silicon-based matrices, SCC samples fabricated by mixing Fe powders with other types of elastomers including polyurethane F140 (PU_{F140}), polyurethane FLEXI45 ($PU_{FLEXI45}$), and styrene-ethylene/buthylene-styrene triblock copolymer (SEBS) are tested. We fabricate samples with different elastomer-Fe weight ratios of 1:2 and 1:4, which are denoted as $PU_{F140\text{-}Fe2/4}$, $PU_{FELXI45\text{-}Fe2/4}$, and $SEBS_{Fe2/4}$, respectively. The measured mechanical and electromechanical properties for samples obtained from different batches are summarized in figures S11 and S12, from which we can see that samples with the same elastomer-Fe ratio have a similar Young's modulus and resistivity response to compressive strain. Also, the rupture strain decreases with the increase in Fe content for these SCCs (figure S13), which is similar to SCCs with silicon-based matrices. This set of experiments shows that the ASPP can produce SCCs with

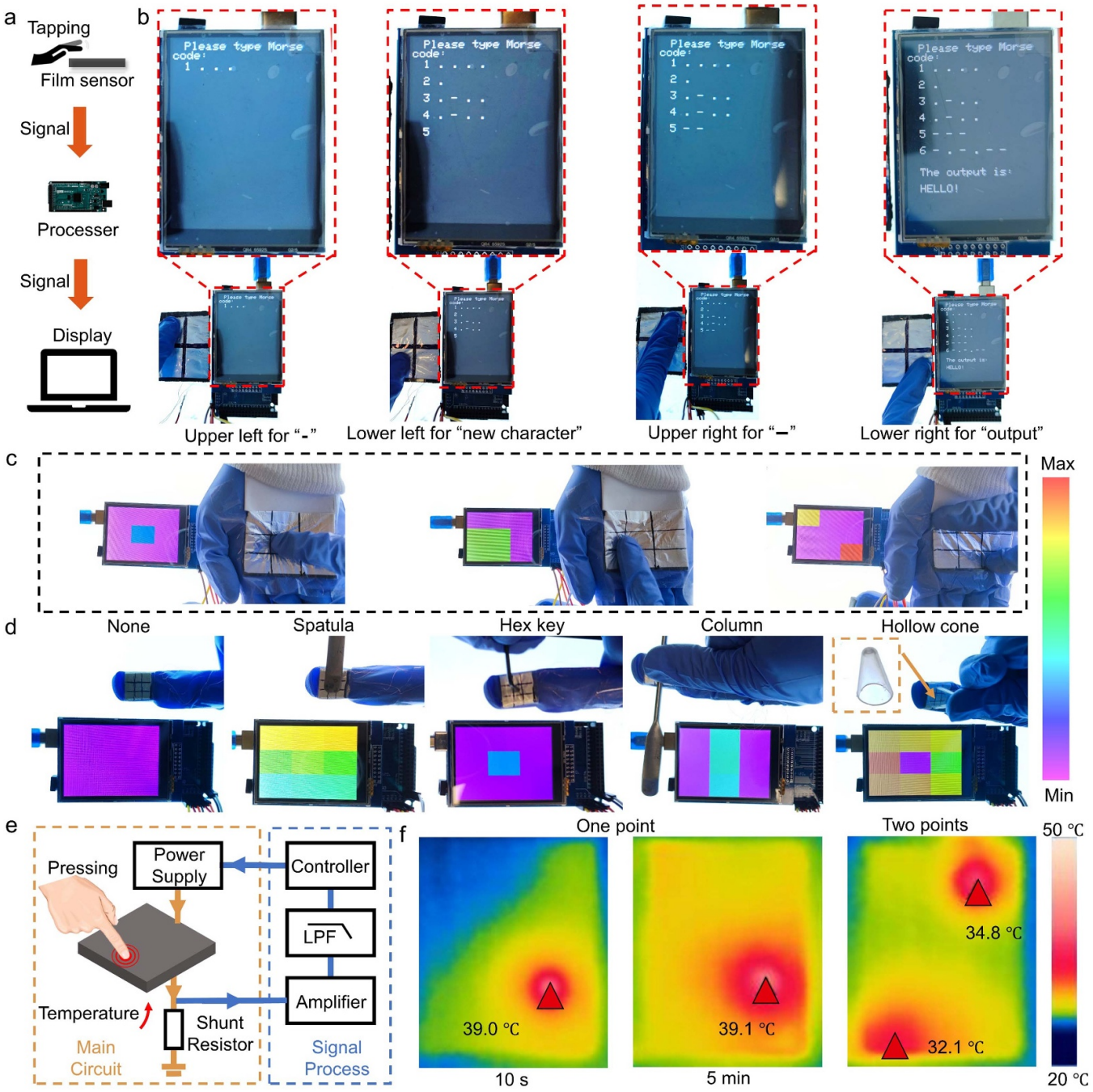

Figure 4. Demonstration of proof-of-concept applications of SCCs. (a) Schematic diagram of a Morse code typing device. (b) Schematic illustrating the function of each block and the demodulation of input signals into output information. (c) Real-time response of a palm tactile device with force sensing. (d) A fingertip tactile device for detecting various objects. (e) Schematic of the operation of a SRHF. (f) Joule heating effect induced on the film by applying local pressure to specific locations.

high batch-to-batch consistency to meet various demands on mechanical and electrical properties.

2.4. Demonstration of proof-of-concept applications for SCCs

Benefiting from the on-demand production of SCCs using the ASPP, several intelligent devices utilizing the SCCs are demonstrated. Tactile devices can be realized using the SCC harnessing its high sensitivity to pressure. To demonstrate this, we design a tapping sensor to translate information via Morse code. The signal transmission diagram of the Morse code display is shown in figure 4(a). Upon tapping the film sensor, the signal will be transferred to the processor to demodulate the information before sending it to the display. Figure 4(b) displays the translation of the input Morse code into the word 'HELLO!'. Using the same principle, tactile devices for spatial and temporal detection of force distribution on a palm and

a fingertip are developed. The palm tactile device includes a pad with nine E_{Fe4} sensors and a display to show the signal in real time. Figure 4(c) shows the response signals when touching different areas of the palm. The force exerted on the sensor can be reflected by the corresponding color on the screen in real time. Similarly, a smaller tactile device for sensing forces exerted on a fingertip is designed, as shown in figure 4(d). The tactile device is able to sense the object's shape when touching a spatula, a hex key, a column, and a hollow cone (figure 4(d)). Assembling palm and fingertip tactile sensors in customized ways could help establish a wearable electronic system for soft robotics and motion detection.

Furthermore, owing to the high thermal/electrical conductivity and high sensitivity to pressure of SCCs with EGaIn microdroplets embedded [32], we demonstrate a self-regulated heating film (SRHF) using $E_{Fe4\text{-}LM}$ which can locally induce the Joule heating effect upon applying pressure. Figure 4(e) shows the heating mechanism of the SRHF. We use a shunt resistor to monitor the current in the main circuit and output feedback to the controller to regulate the power input to the SRHF. When applying local pressure to the SRHF, the resistance under the pressed area drops sharply, leading to a surge of electrical current that can generate heat. The desired maximum temperature is capped by adjusting the maximum current threshold. The left two images in figure 4(f) show the temperature at the same pressed point at 10 s and 5 min, respectively, indicating that the SRHF can heat up to 39 °C in just a few seconds and maintain the desired temperature instead of overheating in the area. Pressure can be applied to multiple areas to generate more hot spots (figure 4(f)). The SRHF is capable of rapidly generating local hot spots with controlled temperatures depending on the applied pressure, highlighting its potential in making wearable heating devices with high power efficiency.

3. Conclusion

In summary, we develop an automatic and integrated platform for the versatile fabrication of SCCs with batch-to-batch consistency. The ASPP consists of modules for TC, mixing, vacuuming, and curing, which can be readily assembled and disassembled to fulfil customized fabricating manners. Fabrication of SCCs with single and hybrid fillers is demonstrated using different types of fillers and elastomeric matrices. In addition, the capability of the platform for making porous PDMS is presented. More importantly, we find that the SCCs fabricated using the ASPP maintain similar electrical and mechanical properties in different batches. Finally, we demonstrate applications of the produced SCCs in making tactile devices for translating Morse codes, spatial and temporal pressure sensing, and generating local heating spots. We anticipate that the ASPP will facilitate the on-demand fabrication of SCCs with good quality control to broaden their application scenarios, allowing interdisciplinary innovations for advancing research in soft robotics, wearable devices, and flexible electronics.

4. Experimental section

4.1. Chemicals and reagents

EGaIn (75.5 wt% Ga and 24.5 wt% In) LM, iron (325 mesh) Poly (dimethylsiloxane) (monohydroxy terminated), glycerol, polysorbate 20, Styrene-ethylene-butylene-styrene (SEBS), Tetrahydrofuran (THF) and fluorescein sodium salt were purchased from Sigma Aldrich, Australia. Polyurethane F140 and polyurethane FLEXI45 were purchased from BARNES PRODUCTS PTY LTD, Australia. SYLGARD™ 184 Silicone Elastomer Kit was purchased from Dow Corning, America. Ecoflex™ 00-31 Near Clear™ was purchased from Smooth-On, Australia.

4.2. Instruments, controls, and fabrication

Thermoelectric pads (Peltier), stepper motors (42BYGH34), A4988 stepper motor driver carriers, aluminum profiles, guide rails, a vacuum pump (∼80 kPa), an Arduino MEGA 2560 microcontroller module, an eight digital display (3461BS), two H-Bridges (IBT- 2), a thin-film-transistor liquid crystal display (TFT LCD), and a thermocouple (MAX6675) were purchased online. The container, slidable holder, and curing molds were manufactured using a 3D printer (Anycubic, China). The Arduino output signals into (1) three A4988 carriers to control the agitator position, (2) two H-bridges to control the agitator rotation speed and direction as well as the temperature of the container, and (3) a metal oxide semiconductor field effect transistor (MOSFET) to control the vacuum pump to degas.

When preparing SCCs, we first weighed the raw materials and added them to the container. Then, ASPP was activated to fabricate SCCs following the steps of: (1) stirring the mixture using a customized agitator (rotating speed up to 9000 rpm) for 5 min, (2) vacuuming the mixture for 15 min to remove air bubbles using the vacuum pump, and (3) maintaining the temperature of the container at 50 °C for 6 h to cure the SCCs. It is worth mentioning that the preparation of $SEBS_{Fe}$ requires adding THF to dissolve it and volatilizing THF after that.

When preparing the porous $P_{Fe4\text{-}LM}$, we first weighed the PDMS base, curing agent, monohydroxy terminated PDMS, Fe powder, and EGaIn with weight ratio of 15:2:5:88:22 and added them in the container. Then, ASPP was activated to fabricate it following the steps: (1) stirring the mixture using a customized agitator (rotating speed up to 9000 rpm) for 3 min. (2) Adding one quarter volume of the mixture of glycerol and polysorbate 20 into the container to further stir for 5 min. (3) Maintaining the temperature of the container at 50 °C for 6 h to cure the mixture. Finally, the porous $P_{Fe4\text{-}LM}$ was further soaked into water for 24 h to completely dissolve glycerol inside.

When preparing the porous sponge, we first weighed glycerol and polysorbate 20 and added them in the container. Then, ASPP made it following the steps: (1) stirring the mixture for 3 min. The container was surrounded by water to

provide humid environment. (2) Adding other raw materials into the container to further stir for 10 min. (3) Maintaining the temperature of the container at 50 °C for 6 h to cure PDMS. Finally, the cured PMDS was further soaked into water for 24 h to completely dissolve glycerol in the PDMS.

4.3. Characterization

SEM images and EDS element mapping were obtained by a EBPG 5200 SEM. Optical microscope images were obtained by an Olympus CKX53 microscope. Thermal images were filmed by a thermal imaging camera (FLIR E5). Mechanical properties were obtained by a MTS Landmark 370.02 hydraulic load frame. Electrical resistances were measured by a Stanley Digital Multimeter.

Data availability statement

The data cannot be made publicly available upon publication because they are not available in a format that is sufficiently accessible or reusable by other researchers. The data that support the findings of this study are available upon reasonable request from the authors.

Author contributions

S-Y T, H L and W L conceived the idea. H L, X H, Q Z, T C, G Y, and Y Z carried out the experiments. The manuscript was written through contributions of all authors. S-Y T, R Q and W L supervised the project. All authors have given approval to the final version of the manuscript.

Conflict of interest

The authors declare no competing financial interest.

ORCID iDs

Qingtian Zhang https://orcid.org/0000-0002-7704-7427
Xumin Huang https://orcid.org/0000-0003-0139-3873
Tim Cole https://orcid.org/0000-0002-0221-1560
Weihua Li https://orcid.org/0000-0002-6190-8421
Shi-Yang Tang https://orcid.org/0000-0002-3079-8880

References

[1] Shojaeian M, Caldag H O, Bozkurt A and Yesilyurt S 2022 Fabrication of magnetic helical microribbons made of nickel thin films sandwiched between silicon nitride layers for microswimming applications *Nanotechnology* **34** 015301
[2] Lu Y and Tong L 2022 Optimal design and experimental validation of 3D printed soft pneumatic actuators *Smart Mater. Struct.* **31** 115010
[3] Hong H, Jung Y H, Lee J S, Jeong C, Kim J U, Lee S, Ryu H, Kim H, Ma Z and Kim T-I 2019 Anisotropic thermal conductive composite by the guided assembly of boron nitride nanosheets for flexible and stretchable electronics *Adv. Funct. Mater.* **29** 1902575
[4] Kwon C *et al* 2020 Self-bondable and stretchable conductive composite fibers with spatially controlled percolated Ag nanoparticle networks: novel integration strategy for wearable electronics *Adv. Funct. Mater.* **30** 2005447
[5] Lu C, Wang X, Shen Y, Wang C, Wang J, Yong Q and Chu F 2022 Liquid-free, anti-freezing, solvent-resistant, cellulose-derived ionic conductive elastomer for stretchable wearable electronics and triboelectric nanogenerators *Adv. Funct. Mater.* **32** 2207714
[6] Qiu W, Zhang C and Zhang Q 2022 Versatile copolymer for stretchable and self-healable liquid-free ionic conductive elastomers *ACS Appl. Mater. Interfaces* **14** 42578–85
[7] Zhang H, Guo J, Wang Y, Sun L and Zhao Y 2021 Stretchable and conductive composite structural color hydrogel films as bionic electronic skins *Adv. Sci.* **8** 2102156
[8] Andrés Castán J-M, Mwalukuku V M, Riquelme A J, Liotier J, Huaulmé Q, Anta J A, Maldivi P and Demadrille R 2022 A stretchable and adhesive composite hydrogel containing PEDOT:PSS for wide-range and precise motion sensing and electromagnetic interference shielding and as a triboelectric nanogenerator *Mater. Chem. Front.* **6** 2994–3005
[9] Park S, Mondal K, Treadway R M III, Kumar V, Ma S, Holbery J D and Dickey M D 2018 Silicones for stretchable and durable soft devices: beyond Sylgard-184 *ACS Appl. Mater. Interfaces* **10** 11261–8
[10] Yao B *et al* 2021 Soft liquid-metal/elastomer foam with compression-adjustable thermal conductivity and electromagnetic interference shielding *Chem. Eng. J.* **410** 128288
[11] Kim D C, Shim H J, Lee W, Koo J H and Kim D-H 2020 Material-based approaches for the fabrication of stretchable electronics *Adv. Mater.* **32** 1902743
[12] Guo R, Wang X, Chang H, Yu W, Liang S, Rao W and Liu J 2018 Ni-GaIn amalgams enabled rapid and customizable fabrication of wearable and wireless healthcare electronics *Adv. Eng. Mater.* **20** 1800054
[13] Yang J C, Lee S, Ma B S, Kim J, Song M, Kim S Y, Kim D W, Kim T-S and Park S 2022 Geometrically engineered rigid island array for stretchable electronics capable of withstanding various deformation modes *Sci. Adv.* **8** eabn3863
[14] He X, Wu J, Xuan S, Sun S and Gong X 2022 Stretchable and recyclable liquid metal droplets embedded elastomer composite with high mechanically sensitive conductivity *ACS Appl. Mater. Interfaces* **14** 9597–607
[15] Shen Z, Zhu X, Majidi C and Gu G 2021 Cutaneous ionogel mechanoreceptors for soft machines, physiological sensing, and amputee prostheses *Adv. Mater.* **33** 2102069
[16] Yang J *et al* 2022 Skin-inspired capacitive stress sensor with large dynamic range via bilayer liquid metal elastomers *Adv. Mater. Technol.* **7** 2101074
[17] Yun G, Tang S-Y, Lu H, Zhang S, Dickey M D and Li W 2021 Hybrid-filler stretchable conductive composites: from fabrication to application *Small Sci.* **1** 2000080
[18] Tutika R, Zhou S H, Napolitano R E and Bartlett M D 2018 Mechanical and functional tradeoffs in multiphase liquid metal, solid particle soft composites *Adv. Funct. Mater.* **28** 1804336
[19] Wu S, Cui Z, Baker G L, Mahendran S, Xie Z and Zhu Y 2021 A biaxially stretchable and self-sensing textile heater using silver nanowire composite *ACS Appl. Mater. Interfaces* **13** 59085–91
[20] Krawczyk K K *et al* 2021 Self-reducing silver ink on polyurethane elastomers for the manufacture of thin and highly stretchable electrical circuits *Chem. Mater.* **33** 2742–55
[21] Choi S *et al* 2018 Highly conductive, stretchable and biocompatible Ag–Au core–sheath nanowire composite for

wearable and implantable bioelectronics *Nat. Nanotechnol.* **13** 1048–56
[22] Yun G *et al* 2021 Liquid metal hybrid composites with high-sensitivity and large dynamic range enabled by micro- and macrostructure engineering *ACS Appl. Polym. Mater.* **3** 5302–15
[23] Niu S, Wang S, Yan Q, Han Z, Lou X, Li Q, Wang Z, Leung C W and Qu S 2021 Tunable piezoresistivity of low percolation threshold micro-nickel wires/PDMS conductive composite regulated by magnetic field *J. Mater. Chem.* C **9** 5908–19
[24] Chen Y-F, Huang M-L, Cai J-H, Weng Y-X and Wang M 2022 Piezoresistive anisotropy in conductive silicon rubber/multi-walled carbon nanotube/nickel particle composites via alignment of nickel particles *Compos. Sci. Technol.* **225** 109520
[25] Yun G, Tang S-Y, Sun S, Yuan D, Zhao Q, Deng L, Yan S, Du H, Dickey M D and Li W 2019 Liquid metal-filled magnetorheological elastomer with positive piezoconductivity *Nat. Commun.* **10** 1–9
[26] Zhang F, Ren D, Huang L, Zhang Y, Sun Y, Liu D, Zhang Q, Feng W and Zheng Q 2021 3D interconnected conductive graphite nanoplatelet welded carbon nanotube networks for stretchable conductors *Adv. Funct. Mater.* **31** 2107082
[27] Chang S, Lou H, Meng W, Li M, Guo F, Pang R, Xu J, Zhang Y, Shang Y and Cao A 2022 Carbon nanotube/polymer coaxial cables with strong interface for damping composites and stretchable conductors *Adv. Funct. Mater.* **32** 2112231
[28] Han F *et al* 2018 Fabrication of a flexible and stretchable three-dimensional conductor based on Au–Ni@graphene coated polyurethane sponge by electroless plating *J. Mater. Chem.* C **6** 8135–43
[29] Song J, Kim Y, Kang K, Lee S, Shin M and Son D 2022 Stretchable and self-healable graphene–polymer conductive composite for wearable EMG sensor *Polymers* **14** 3766
[30] Zhang D, Liu A, Chang H and Xia B 2015 Room-temperature high-performance acetone gas sensor based on hydrothermal synthesized SnO_2-reduced graphene oxide hybrid composite *RSC Adv.* **5** 3016–22
[31] Gong S, Yap L W, Zhu B and Cheng W 2020 Multiscale soft–hard interface design for flexible hybrid electronics *Adv. Mater.* **32** 1902278
[32] Daeneke T, Khoshmanesh K, Mahmood N, de Castro I A, Esrafilzadeh D, Barrow S J, Dickey M D and Kalantar-zadeh K 2018 Liquid metals: fundamentals and applications in chemistry *Chem. Soc. Rev.* **47** 4073–111
[33] Xin Y, Gao T, Xu J, Zhang J and Wu D 2021 Transient electrically driven stiffness-changing materials from liquid metal polymer composites *ACS Appl. Mater. Interfaces* **13** 50392–400
[34] Migliorini L, Piazzoni C, Pohako-Esko K, Di Girolamo M, Vitaloni A, Borghi F, Santaniello T, Aabloo A and Milani P 2021 All-printed green micro-supercapacitors based on a natural-derived ionic liquid for flexible transient electronics *Adv. Funct. Mater.* **31** 2102180
[35] Mao G, Schiller D, Danninger D, Hailegnaw B, Hartmann F, Stockinger T, Drack M, Arnold N and Kaltenbrunner M 2022 Ultrafast small-scale soft electromagnetic robots *Nat. Commun.* **13** 4456
[36] Tutika R, Haque A B M T and Bartlett M D 2021 Self-healing liquid metal composite for reconfigurable and recyclable soft electronics *Commun. Mater.* **2** 64
[37] Hong S Y, Kim M S, Park H, Jin S W, Jeong Y R, Kim J W, Lee Y H, Sun L, Zi G and Ha J S 2019 High-sensitivity, skin-attachable, and stretchable array of thermo-responsive suspended gate field-effect transistors with thermochromic display *Adv. Funct. Mater.* **29** 1807679
[38] Yang P-K, Li X-Y, Yang X-Y, Li G-W, Hu Z-J, Huang L and Wu Y-P 2022 Lightweight liquid metal-elastomer foam with smart multi-function *Adv. Funct. Mater.* **32** 2205167
[39] Park J, Kim I, Yun J and Kim D 2021 Liquid-metal embedded sponge-typed triboelectric nanogenerator for omnidirectionally detectable self-powered motion sensor *Nano Energy* **89** 106442
[40] Huang Y, Yu B, Zhang L, Ning N and Tian M 2019 Highly stretchable conductor by self-assembling and mechanical sintering of a 2D liquid metal on a 3D polydopamine-modified polyurethane sponge *ACS Appl. Mater. Interfaces* **11** 48321–30
[41] Cai S *et al* 2022 Soft liquid metal infused conductive sponges *Adv. Mater. Technol.* **7** 2101500
[42] Ning N, Huang W, Liu S, Zhao Q, Zou H, Yu B, Tian M and Zhang L 2019 Highly stretchable liquid metal/polyurethane sponge conductors with excellent electrical conductivity stability and good mechanical properties *Composites* B **179** 107492
[43] Markvicka E J, Bartlett M D, Huang X and Majidi C 2018 An autonomously electrically self-healing liquid metal–elastomer composite for robust soft-matter robotics and electronics *Nat. Mater.* **17** 618–24
[44] Liao M, Liao H, Ye J, Wan P and Zhang L 2019 Polyvinyl alcohol-stabilized liquid metal hydrogel for wearable transient epidermal sensors *ACS Appl. Mater. Interfaces* **11** 47358–64
[45] Mou L, Qi J, Tang L, Dong R, Xia Y, Gao Y and Jiang X 2020 Highly stretchable and biocompatible liquid metal-elastomer conductors for self-healing electronics *Small* **16** 2005336
[46] Xin Y, Peng H, Xu J and Zhang J 2019 Ultrauniform embedded liquid metal in sulfur polymers for recyclable, conductive, and self-healable materials *Adv. Funct. Mater.* **29** 1808989
[47] Ma Z *et al* 2021 Permeable superelastic liquid-metal fibre mat enables biocompatible and monolithic stretchable electronics *Nat. Mater.* **20** 859–68
[48] Neumann T V and Dickey M D 2020 Liquid metal direct write and 3D printing: a review *Adv. Mater. Technol.* **5** 2000070
[49] Lu H, Tang S-Y, Dong Z, Liu D, Zhang Y, Zhang C, Yun G, Zhao Q, Kalantar-Zadeh K and Qiao R 2020 Dynamic temperature control system for the optimized production of liquid metal nanoparticles *ACS Appl. Nano Mater.* **3** 6905–14
[50] Chen S, Wang H-Z, Zhao R-Q, Rao W and Liu J 2020 Liquid metal composites *Matter* **2** 1446–80
[51] Yang J *et al* 2020 Ultrasoft liquid metal elastomer foams with positive and negative piezopermittivity for tactile sensing *Adv. Funct. Mater.* **30** 2002611
[52] Hong S, Jung Y, Yen R, Chan H F, Leong K W, Truskey G A and Zhao X 2014 Magnetoactive sponges for dynamic control of microfluidic flow patterns in microphysiological systems *Lab. Chip* **14** 514–21
[53] Thurgood P, Baratchi S, Szydzik C, Zhu J Y, Nahavandi S, Mitchell A and Khoshmanesh K 2018 A self-sufficient micro-droplet generation system using highly porous elastomeric sponges: a versatile tool for conducting cellular assays *Sens. Actuators* B **274** 645–53
[54] Yun G, Cole T, Zhang Y, Zheng J, Sun S, Ou-Yang Y, Shu J, Lu H, Zhang Q and Wang Y 2023 Electro-mechano responsive elastomers with self-tunable conductivity and stiffness *Sci. Adv.* **9** eadf1141
[55] Wan H, Gao K, Li S, Zhang L, Wu X, Wang X and Liu J 2019 Chemical bond scission and physical slippage in the Mullins effect and fatigue behavior of elastomers *Macromolecules* **52** 4209–21